Promoting photocatalytic CO_2 reduction with a molecular copper purpurin chromophore

Huiqing Yuan[1], Banggui Cheng[1], Jingxiang Lei[1], Long Jiang [1] & Zhiji Han [1✉]

CO_2 reduction through artificial photosynthesis represents a prominent strategy toward the conversion of solar energy into fuels or useful chemical feedstocks. In such configuration, designing highly efficient chromophores comprising earth-abundant elements is essential for both light harvesting and electron transfer. Herein, we report that a copper purpurin complex bearing an additional redox-active center in natural organic chromophores is capable to shift the reduction potential 540 mV more negative than its organic dye component. When this copper photosensitizer is employed with an iron porphyrin as the catalyst and 1,3-dimethyl-2-phenyl-2,3-dihydro-1H-benzo[d]imidazole as the sacrificial reductant, the system achieves over 16100 turnover number of CO from CO_2 with a 95% selectivity (CO vs H_2) under visible-light irradiation, which is among the highest reported for a homogeneous noble metal-free system. This work may open up an effective approach for the rational design of highly efficient chromophores in artificial photosynthesis.

[1] MOE Key Laboratory of Bioinorganic and Synthetic Chemistry, School of Chemistry, Sun Yat-sen University, Guangzhou 510275, China.
✉email: hanzhiji@mail.sysu.edu.cn

A rtificial photosynthesis (AP) represents an appealing
strategy for the conversion of solar energy into stored
chemical potential energy[1,2]. Inspired by natural photo-
synthesis, photocatalytic reduction of CO_2 to value-added che-
micals (such as CO, CH_3OH, and $C_{\geq 2}$ products) is a viable
solution to obtain sustainable energy in closing the anthropogenic
carbon cycle[3–7]. Several approaches are available for photo-
chemical reduction of CO_2 to access fuels or chemical
precursors[8]. Homogeneous AP systems usually offer distinct
advantages with respect to structural optimization and product
selectivity[9]. For example, the reduction potentials of all compo-
nents can be finely tuned through functional group manipulation
to facilitate efficient light-driven electron transfer[10]. In a typical
homogeneous AP system, a photosensitizer (PS) is a key com-
ponent responsible for light-harvesting and photochemical
reactions[10,11]. To achieve a high activity in photocatalytic CO_2
conversion, it is essential to develop satisfactory photosensitizers
that have large absorption cross sections in the visible region and
are capable of promoting efficient multiple electron transfer
processes. Recent studies on precious metal-based PS (such as Ru,
Ir, and Re) have shown good activity for CO_2 reduction[12–25].
However, molecular chromophores comprising earth-abundant
elements usually give relatively low turnover numbers (TONs),
which is a significant limitation in developing inexpensive AP
systems[26–29]. Thus, developing highly efficient noble-metal-free
PS for CO_2 conversion remains a persistent challenge for the
scientific community.

Anthracene organic dyes, which is an emerging group of inex-
pensive PS with high molar absorption coefficients in the visible
region, have demonstrated to have good stability in photocatalytic
CO_2 reduction[30]. However, the activity of these photocatalytic
systems is much lower than the ones using metal-based photo-
sensitizers, due to the inefficiency in multiple electron transfer to
the catalyst[11,31]. The system containing 9-cyanoanthracene as the
PS and an iron(0) tetrapenylporphyrin as the catalyst produces CO
with a turnover frequency (TOF) of ~1.5 h^{-1}[32]. Since 2016, pur-
purin (PP) (the main coloring matter in natural madder) has been
studied as one of the most active organic photosensitizers for CO_2
reduction when coupled with a variety of metal catalysts[33–35],
achieving TON_{CO} as high as 1365 (TOF ~ 300 h^{-1}) with respect to
the catalyst[33]. Recently, because of the highly luminescent and
tunable redox properties, copper diamine photosensitizers have
shown promising activities in driving the reduction of CO_2[12,36].
Ishitani et al. have shown that dimeric Cu complexes with het-
eroleptic diimine and phosphine ligands are effective photo-
sensitizers to exhibit 273 turnovers of CO in 12 h[37]. The systems
employed various copper diimine diphosphine complexes as the
photosensitizers, Fe[37–39], Co[40], Ni[41], or Mn[42,43] metal complexes as
the catalysts, and 1,3-dimethyl-2-phenyl-2,3-dihydro-1H-benzo[d]
imidazole (BIH) as the sacrificial electron donor that produced CO
up to 2680 turnovers under optimal conditions[40]. While Cu diimine
photosensitizers exhibit relatively higher activities in photocatalytic
CO_2 reduction than organic PS, they require much higher energetic
light irradiation owing to their absorption spectra centered at the
UV region[36]. To facilitate fast electron transfer between an electron
donor and acceptor, various PS-catalyst dyads have been
studied[8,44,45]. This strategy has shown an increase in activities from
the linked systems, with TON_{co} as high as 4347[46]. However, these
studies were performed with precious metals, and fastback electron
transfer from the catalyst to the PS is usually observed in these
dyads, which could hinder efficient charge separation.

In this work, we report a highly active copper purpurin PS for
visible-light-driven CO_2 reduction to CO in a noble metal-free
system (Fig. 1). By coordinating a redox-active Cu center directly
to the redox noninnocent catecholate motifs[47] on natural organic
dyes, we create a simple yet highly efficient PS to facilitate

challenging multielectron reductions. Electrochemical studies
reveal that the incorporation of Cu in purpurin produces a much
more reducing PS for catalysis. When coupled with a Fe por-
phyrin as the catalyst and BIH as the sacrificial electron donor,
this Cu PS significantly boosts the photocatalytic activity (>50-
fold) of the system for CO_2 reduction compared with its organic
dye component. This homogeneous system achieves over 16,100
turnovers of CO and a TOF_{max} of 7650 per hour with a 95%
selectivity (CO vs H_2), which is the highest for homogeneous
noble metal-free systems. Importantly, this system demonstrates a
>fourfold increase in TON_{co} compared to the most active noble
metal-based systems using metal porphyrin catalysts[48].

Results and discussion

Preparation and characterization of CuPP. As outlined in Fig. 2,
Cu purpurin complex was prepared by heating $Cu(NO_3)_2$, PP (2.0
equiv), and $NaHCO_3$ (4.0 equiv) in dimethylformamide (DMF) at
100 °C for 24 h. X-ray diffraction (XRD, *vide infra*) quality single
crystals of the isolated compound have not been obtained due to
its low solubility in most organic solvents. Electrospray ionization
mass spectrometry (ESI-MS) and elemental analysis of this pro-
duct suggest the formation of a $Na_2Cu(PP)_2$ complex (Supple-
mentary Fig. 1a). Cation exchange of this compound was carried
out in water with tetrabutylammonium bromide (TBABr) (2.0
equiv). Recrystallization of the resulting $(TBA)_2Cu(PP)_2$ (CuPP)
by slow diffusion of diethyl ether into an acetonitrile solution
gave dark-red crystals suitable for single-crystal XRD studies.

Polyhydroxy-9,10-anthracenediones have been used for the
detection of various transition metal ions[49,50]; however, solid-
state structures of these complexes are very rare[51,52]. Figure 2
shows the crystal structure of a Cu purpurin complex. In this
structure, the Cu center displays a square planar geometry and is
coordinated with the 1- and 2-hydroxyl groups on the 9,10-
anthracenediones, which is different from the 2,3-oxygen chelates
proposed in the literature based on theoretical calculation[53]. The
Cu–oxygen distances (Cu–O1 = 1.927(2) and Cu–O2 = 1.917(2)
Å) are similar to the Cu–O bonds reported for Cu(II) catecholate
compounds in the literature (Supplementary Table 1). This
evidence along with the electronic charge balancing, and
paramagnetic proton resonances in the ^1H NMR spectra
(Supplementary Figs. 3 and 4) are all consistent with the
assignment of a Cu(II) center in CuPP. The catecholate
carbon–oxygen distances (C2–O2 = 1.295(3) and C1–O1 =
1.303(3) Å) are identical to those found for a Ru
$(CO)_2(PBu_3)_2(1,2,3$-trihydroxy-9,10-anthracenedione) complex,
suggesting they are single C–O bonds[51]. In the anthraquinone
moieties, the C4–O3 distance (1.239(3) Å) is typical a double
bond, while the other double bond C11–O4 (1.274(3) Å) is
elongated due to the hydrogen bonding interaction with its
adjacent hydroxyl.

The UV–vis absorption spectra of CuPP and PP were
measured at room temperature in DMF (Fig. 3a). CuPP displays
a much stronger visible absorption profile than PP, with intense
absorption that tails to almost 650 nm (Fig. 3a). The significant
red shift of the maximum absorption band at 478 nm (ε = 9.94 ×
10^3 M^{-1} cm^{-1}) of PP to 566 nm (ε = 3.85 × 10^4 M^{-1} cm^{-1}) of
CuPP is probably due to the generation of dianion of
hydroxyanthraquinone and an induction effect from the Cu(II)
center. Linear Beer's law at two wavelengths (278 and 566 nm)
applied for the range of concentrations used in CuPP (Supple-
mentary Fig. 10), suggesting negligible solute–solute interactions.

Because the UV–vis spectrum of CuPP exhibits identical
features as compared to the dianion form of PP in the visible
region[54], the absorption band at 566 nm is assigned to the charge
transfer band on the PP ligands. The incorporation of Cu(II)
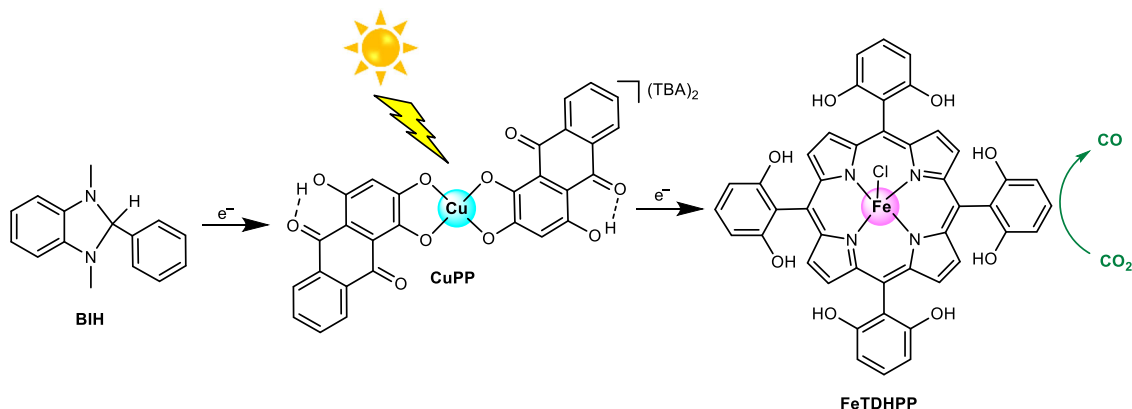
Fig. 1 Illustrative scheme of the photocatalytic CO$_2$ reduction system. BIH is the sacrificial reductant, and CuPP is the photosensitizer, and FeTDHPP is the catalyst investigated in this study.
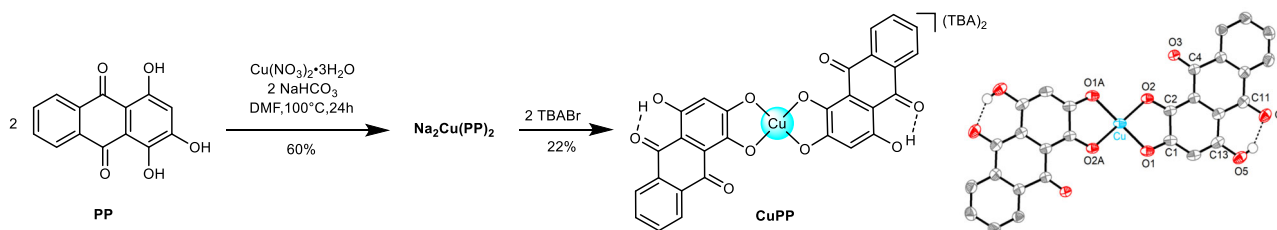
Fig. 2 Synthetic route for Cu purpurin complexes and crystal structure of CuPP. Thermal ellipsoids are shown at the 50% probability level. Parts of hydrogen atoms and TBA cations are not shown for clarity.
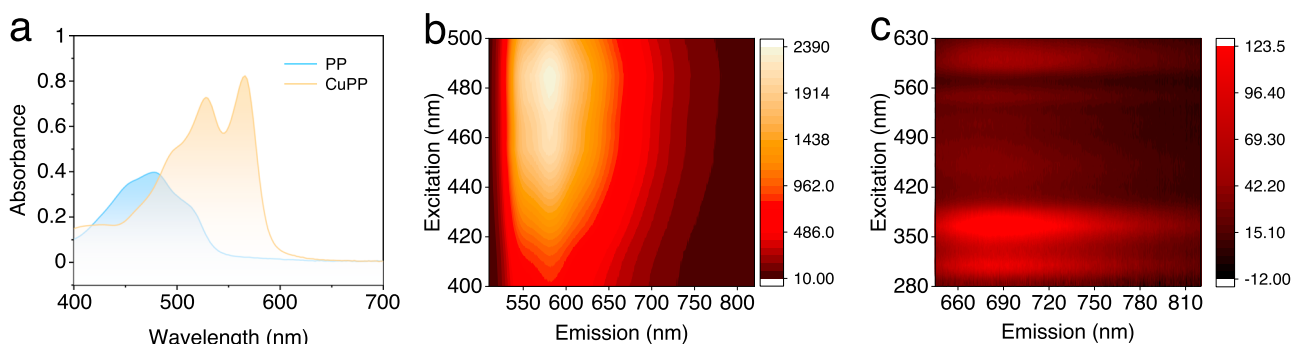

Fig. 3 Absorption and emission profiles of CuPP and PP. a UV–vis analysis of CuPP (20 µM, orange) and purpurin (40 µM, blue) in DMF; excitation and emission spectra of PP (**b**) and CuPP (**c**) at different wavelengths at 298 K in DMF. Source data are provided as a Source Data file.

enhances this charge transfer process by showing a much higher molar extinction coefficient (Supplementary Fig. 10). The photoluminescence quantum yield for CuPP (8.2×10^{-3}) is lower than that of PP (2.7×10^{-2}) (Supplementary Table 2). Instead, Grazia et al. observed an increase of the fluorescence intensity when adding Al(III) to PP[55]. Short stokes shifts of emissions were observed for both Al-PP and PP, and their excitation spectra are comparable with the absorption spectra (Supplementary Fig. 11a)[55,56], suggesting that these compounds undergo relatively low structural reorganization between the ground and excited states. In contrast, CuPP displays structureless emission at 693 nm with a large bathochromic shift. The distinct absorption and emission spectra of CuPP (Supplementary Fig. 12b) indicate a significant structural change in its excited state. Since Cu(I) complexes tend to adopt distorted geometries compared to their Cu(II) analogs[40,57–60], the nature of the emission of CuPP is likely from a Cu(I) excited state generated from a LMCT process. Excitation–emission spectra (Fig. 3b, c) show that the emission of CuPP is most intense when excited at 375 nm. The excited-state

lifetimes are on the nanosecond timescale for both CuPP ($\tau = 0.98$ ns) and PP ($\tau = 1.1$ ns)[35,54].

Electrochemical analysis of CuPP. Figure 4 shows the cyclic voltammograms (CVs) of CuPP and PP in DMF solution containing 0.1 M tetrabutylammonium hexafluorophosphate (TBAPF$_6$). Indeed, the incorporation of a Cu(II) center into PP creates additional reduction events. CuPP displays three irreversible reduction potentials at −1.05, −1.50, and −1.69 V vs SCE. The most negative redox couple of CuPP at −1.75 V is 540 mV more negative than the PP^{2-}/PP$^-$ couple (Fig. 4a)[33]. Square wave voltammetry (SWV) reveals that there are four successive reductions, which correspond to 2, 1, 1, and 2 electron processes (Supplementary Fig. 17).

To explore the electron requirements for photocatalytic systems, further CV experiments were performed to study the electrocatalytic activity for CO$_2$ reduction. Under an atmosphere of CO$_2$, CuPP shows a quasi-reversible reduction wave at −0.97 V and a catalytic wave that starts to appear below −1.89 V as
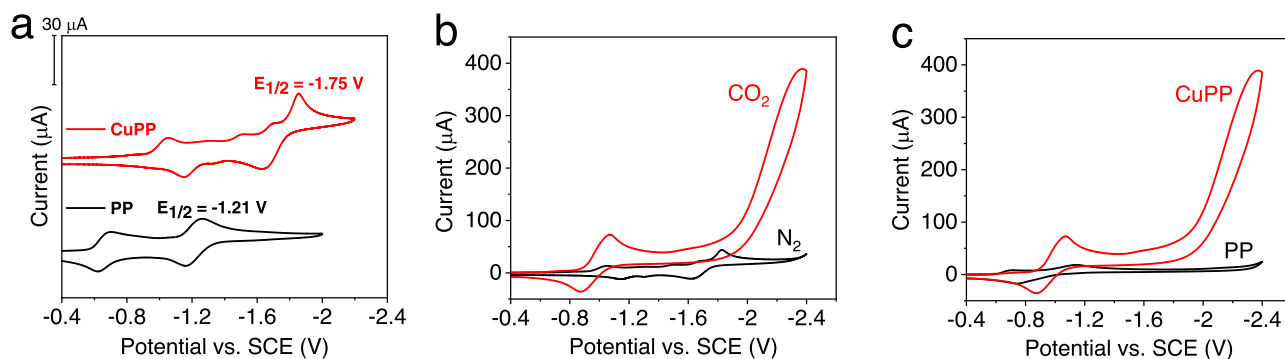
Fig. 4 Electrochemical data of CuPP and purpurin under N_2 or CO_2. Experiments were performed in DMF containing 0.1 M $TBAPF_6$ at scan rate 0.1 V/s: **a** 1 mM CuPP (red) and 1 mM PP (black) under N_2; **b** 1 mM CuPP under N_2 (black) and CO_2 (red); **c** 1 mM CuPP (red) and 1 mM PP (black) under CO_2. Source data are provided as a Source Data file.
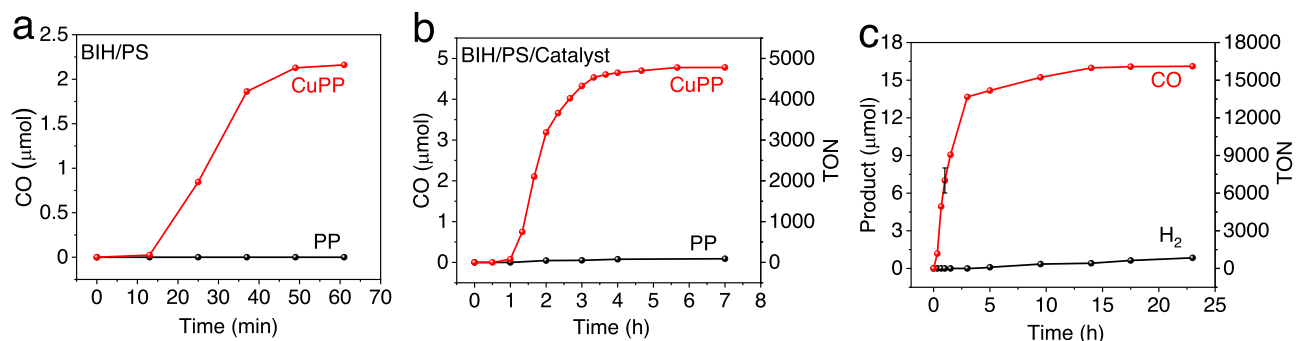
Fig. 5 Photocatalytic CO_2 reduction. Experiments were performed in CO_2-saturated DMF solution containing **a** 0.1 mM CuPP (red) or 0.2 mM PP (black), and 100 mM BIH; **b** 0.2 mM PP (black) or 0.1 mM CuPP (red), 0.2 µM FeTDHPP, and 10 mM BIH; **c** 0.1 mM CuPP, 0.2 µM FeTDHPP, and 100 mM BIH. Error bar (95% confidence interval based on three runs) is included at the 1-h point, which is the typical error in the measurement (14%). Source data are provided as a Source Data file.

compared to no observation of current enhancement in N_2 (Fig. 4b), suggesting that CuPP could act as a CO_2 reduction catalyst. CV control experiments for PP and electrolyte solution show little current enhancement at the same potentials in the presence of CO_2 (Fig. 4c). The integrals of SWV show a total of four-electron reduction at −1.13 V prior to the catalytic current (Supplementary Fig. 17). The different electrochemical profiles observed for CuPP in the presence of CO_2 and N_2 indicate that the four quinone moieties on the PP ligands undergo four-electron reductions and four complexations of CO_2 to generate carbonates. In fact, a similar observation for 9,10-anthracenediones has been reported in the literature[61]. Controlled potential coulometry experiments, performed at −1.89 V (vs SCE) in CO_2-saturated DMF, show that CO is the main gas product with a faradaic yield of 17% and only a negligible amount of H_2 generated (Supplementary Fig. 20). In a control experiment without CuPP, there is little CO or H_2 produced. These data confirm that the observed current enhancement of CuPP corresponds to CO_2 reduction, not proton reduction.

Photocatalytic CO_2 reduction. The electrocatalytic CO_2 reduction properties of CuPP (see Fig. 4) together with its strong absorption in the visible spectral region (Fig. 3) provide strong evidence that CuPP may serve as both photosensitizer and catalyst for CO_2 reduction. Photocatalytic experiments were performed by irradiating CuPP (0.1 mM) in DMF with a white light-emitting diode ($\lambda > 400$ nm) in the presence of BIH (0.1 M) as the sacrificial donor. The amount of gaseous products were monitored in real time using gas chromatography (GC). Figure 5a shows that CuPP-containing system generates CO upon

irradiation with an initial turnover frequency of 4.3 h^{-1}, while there is no CO observed in the control system using PP (2.0 equiv) instead of CuPP (Table 1). However, the rate of CO evolution decreases dramatically after one hour. The disappearance of the color of the reaction mixture after irradiation indicates the decomposition of CuPP.

The activity and stability of photocatalytic CO_2 reduction can be significantly improved with the addition of chloro iron (III) 5, 10, 15, 20-tetrakis (2',6'-dihydroxyphenyl)-porphyrin (FeTDHPP) as the cocatalyst (Fig. 1), which has been shown to be an active electrocatalyst for CO_2 reduction[62]. In a typical experiment, the system containing 0.1 mM CuPP, 0.2 µM FeTDHPP, and 10 mM BIH, produces 4779 TONs of CO/mol of catalyst in 7 h in CO_2-saturated DMF solution (Fig. 5b and Table 1). For comparison, an experiment performed using PP as the PS under the same conditions gives a TON of 88 for CO_2 (Fig. 5b and Table 1), underscoring the importance of CuPP for photocatalytic CO_2 reduction. The CuPP PS can also be generated in situ with the addition of 1:2 ratio of Cu^{2+} and PP. The amount of CO produced with the in situ-generated PS is ~25% lower than that of the system using isolated CuPP (Supplementary Fig. 21a). UV–vis spectra confirm that CuPP can be generated in minutes when mixing Cu^{2+} and PP in the presence of BIH (Supplementary Fig. 21b). Control experiments show that the absence of PS leads to no CO or H_2 production (Supplementary Table 4).

An induction period observed at low BIH concentration disappears as [BIH] increased above 0.1 M (Supplementary Fig. 22), which suggests that the rate of CO production is limited by the concentration of sacrificial donor. At 100 mM concentration of BIH, the activity of CO_2 to CO conversion is further improved, achieving 16,109 TONs in 23 h with an initial TOF of

Table 1 Control and other photocatalytic CO$_2$-reduction experiments.

Entry	PS	[FeTDHPP] (μM)	[BIH] (mM)	Irradiation time (h)	CO (μmol)	H$_2$ (μmol)	TON$_{CO}$	TOF$_{CO}$^{max} (h^{-1})	TON$_{H2}$	Sel$_{CO}$ (%)
1	PP	0.2	10	7	0.088	0	88	45	0	100
2	CuPP	0.2	10	7	4.779	0.27	4779	1356	270	95
3	CuPP	0.2	100	23	16.109	0.843	16109	7650	843	95
4	CuPP	0	100	1	2.2	0	4.4a	4.3	0	100

^{a}Calculated by the equation TONCO = n(CO)/n(CuPP).
Comparison data for the photocatalytic systems in CO$_2$-saturated DMF solution.
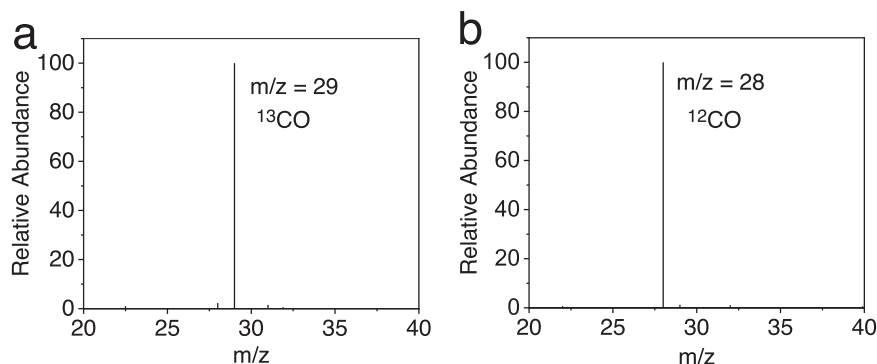
Fig. 6 GC/MS chromatograms of carbon monoxide. Photocatalytic CO$_2$ reduction in ^{13}CO$_2$-saturated (**a**) and ^{12}CO$_2$-saturated (**b**) DMF solutions containing 1.0 μM FeTDHPP, 100 mM BIH, and 0.1 mM CuPP.

7650 h^{-1} with respect to [FeTDHPP] (Fig. 5c and Table 1), which is more than ten times more active than previously reported systems using PP as the PS (Supplementary Table 6). The activity of the photochemical systems was optimized further by varying the [CuPP] and [FeTDHPP]. At fixed concentrations of BIH (100 mM) and FeTDHPP (2 μM), increasing the CuPP concentration increases the overall rate of CO production (Supplementary Fig. 23). However, the rate of CO generation does not increase above 0.1 mM concentration of CuPP. When the CuPP concentration is fixed at 0.1 mM and [FeTDHPP] is varied (Supplementary Fig. 24), the catalyst is most active (on a TON basis) at low concentrations. The total amount of CO evolved increases up to 40 μM FeTDHPP, suggesting that the activity of the system becomes limited by electron transfer to the catalyst. For a system containing 2.0 μM FeTDHPP/100 mM BIH/0.1 mM CuPP, the initial 1 h quantum yield of CO$_2$ to CO conversion at 450 nm was determined at 6.0 ± 0.6%.

Quantification of the gaseous products shows an overall selectivity of 95% for CO and 5% for H$_2$. In the solution, 1.4 μmol formic acid was quantified by high-performance liquid chromatography (HPLC). However, a similar amount (1.5 μmol) of formic acid was detected from the experiment performed under N$_2$, suggesting that formic acid is not generated from CO$_2$ reduction. In fact, formic acid generated from hydrolysis of DMF has been previously reported[63]. To confirm that CO$_2$ is the source of carbon in photolysis, isotopic labeling experiments were performed under an atmosphere of ^{13}CO$_2$. The GC–MS analysis of the gaseous products shows a diagnostic peak of ^{13}CO (Fig. 6). It reveals that CO is derived from CO$_2$ reduction rather than decomposition of other components in the photocatalytic system.

To evaluate the homogeneity of the system, excess of Hg (0.02 mL, 2700 equiv of CuPP) was added to the reaction vessel at the beginning of the experiments, the activity of CO generation remains identical over the course of photolysis (Supplementary Fig. 25). In addition, dynamic light-scattering (DLS) experiments show there is no detectable nanoparticle generated in the reaction mixture before and after CO$_2$ reduction (Supplementary Fig. 26).

These control experiments suggest that there are no Cu colloids generated and the CuPP/FeTDHPP/BIH system stays homogeneous during photocatalytic CO$_2$ reduction.

Several additional experiments were carried out to probe the mechanism of decomposition of the system. When the rate of CO production decreases significantly, fresh solutions containing the same amounts of CuPP, FeTDHPP, BIH, or a mixture of them were added to the reaction mixtures at 23 h. Addition of one or two components leads to much less recovery of the original activity, compared to the one that added all three components (Supplementary Fig. 28). This suggests that the decomposition of all three components occurs during CO generation. Furthermore, absorption of the reaction mixture containing CuPP, FeTDHPP, and BIH in DMF was monitored by UV/vis spectroscopy during photolysis (Supplementary Fig. 29). The intensity of the absorption band at 400 nm, which corresponds to the reductions of PP ligands[35], decreases gradually on the course of irradiation. This confirms that CuPP decomposes during CO$_2$ reduction.

Mechanistic studies. Further experiments were performed to study the photochemical mechanism of CO$_2$ reduction. UV/vis studies show there is no change of the CuPP spectrum with the addition of BIH or FeTDHPP under CO$_2$ (Supplementary Fig. 30), suggesting that the first electron transfer step is initiated by photon absorption. Photochemical steps were studied through fluorescence quenching of CuPP in DMF. The reductive quenching rate constant (using BIH as the quencher) is 9.23×10^9 M^{-1} s^{-1} based on Stern–Volmer equation (Supplementary Fig. 31). A linear plot for the oxidative quenching could not be obtained due to the fact that FeTDHPP has a nonnegligible absorption at both the excitation and emission wavelengths (Supplementary Figs. 32 and 33), which is in agreement with the literature[32,34]. Because [BIH] used in most of our photocatalytic experiments is more than 5 orders of magnitude higher than [FeTDHPP] and the k_q for reductive quenching is at the diffusion-controlled limit, reduction of CuPP* by BIH is expected to be the first electron-transfer step.
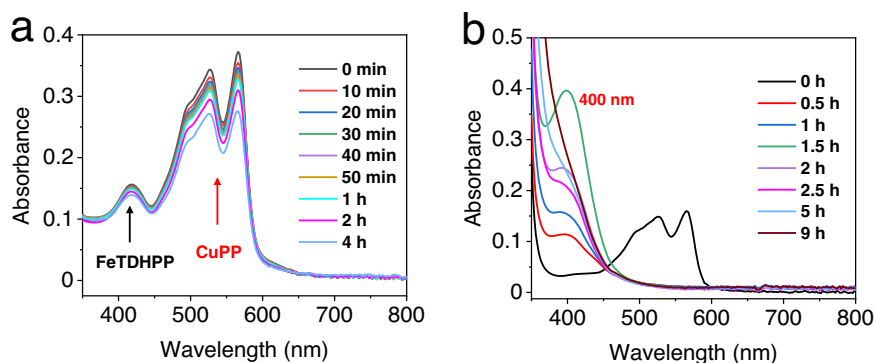
Fig. 7 UV–vis absorption spectra of systems. a In all, 0.01 mM CuPP, 0.5 μM FeTDHPP, 0.1 mM BIH in a quartz cuvette (10-mm path length), and **b** 0.1 mM CuPP, 0.2 μM FeTDHPP, and 100 mM BIH upon irradiation with white LED light. Solutions for (**b**) at different times were transferred and diluted five times with DMF to a quartz cuvette (2-mm path length) under N_2.
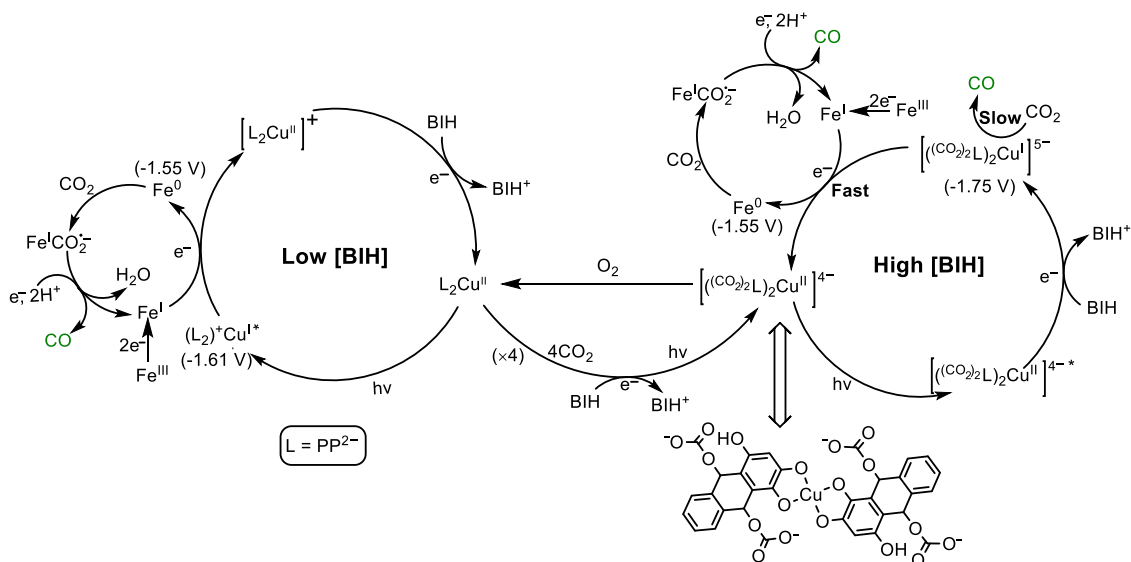
Fig. 8 Proposed reaction scheme. Different pathways for photocatalytic CO_2 reduction are proposed for low [BIH] (left) and high (BIH) (right).

CO generation was observed even at [BIH] as low as 0.1 mM. UV–vis spectra show no generation of the additional absorption band in the visible region during CO_2 reduction (Fig. 7a), indicating CuPP is the active PS at this condition. Since $[L_2Cu^{II}]^-$ (L = PP^{2-}) has a much higher reduction potential (−1.05 V) than that of Fe(I)TDHPP ($E_{1/2}$ = −1.55 V), CO_2 reduction has to proceed through oxidative quenching of $(L_2)^+Cu^{I*}$ (−1.61 V) (Supplementary Table 3) in the photochemical step (Fig. 8). At high [BIH] (100 mM), a yellow species with an absorption band at 400 nm is generated under visible-light irradiation (Fig. 7b). When the reaction mixture is exposed to the air, the solution returns to purple color and over 80% of the original CuPP is recovered based on UV–vis spectra (Supplementary Fig. 34). Electrochemical studies in the presence of CO_2 (Fig. 4b) suggest that CuPP could undergo four steps of reduction and complexation of CO_2 to generate a $[(^{(CO2)2}L)_2Cu^{II}]^{4-}$ species (Fig. 8). In fact, PP has been shown to proceed a two-electron reduction to generate a species at 398 nm during photocatalytic CO_2 reduction[34]. Thus, we conclude that the intermediate with maximum absorption at 400 nm is a $[(^{(CO2)2}L)_2Cu^{II}]^{4-}$ species. $[(^{(CO2)2}L)_2Cu^{I}]^{5-}$ (−1.75 V), generated by further reduction of $[(^{(CO2)2}L)_2Cu^{II}]^{4-}$ through reductive quenching, is corresponding to electron transfer to the Fe catalyst (Fig. 8).

On the basis of a much faster turnover of CO_2 to CO with CuPP compared to PP, electron transfer from the reduced PS to

the catalyst is proposed to be a turnover-limiting step (TOLS) (Fig. 8). Although CuPP is active for photocatalytic CO_2 reduction without an additional catalyst, the significantly lower TOF observed in the CuPP/BIH system clearly shows that this process is much slower than the TOLS of the CuPP/FeTDHPP/BIH system (Fig. 8). Electrochemical studies show that CuPP exhibits a more negative reduction potential (−1.75 V vs SCE) than that of PP (−1.21 V vs SCE). In order to access a previously reported Fe(0) porphyrin intermediate for CO_2 reduction (Fig. 8)[62], CuPP is expected to have a larger driving force for reduction and hence a faster rate for electron transfer to the catalyst than PP.

This work shows an example where an active photosensitizer for CO_2 reduction has been constructed through direct coordination of a redox-active metal center to natural organic dyes. This Cu photosensitizer displays strong visible-light-harvesting and multiple electrochemical properties. In the AP systems using metal porphyrins as the catalysts, CuPP exhibits great photocatalytic activity for CO_2 reduction when compared with previously reported homogeneous photosensitizers, even including the noble metal ones (Supplementary Tables 5–8). For example, the CuPP/FeTDHPP system achieves over 16,100 turnovers of CO with a maximum TOF of 7650 h^{-1}, which is two orders of magnitude more than a reported Ir(ppy)$_3$/FeTDHPP system (TON = 140 in 55 h)[32]. This work not only

paves the way to improve CO_2 to CO conversion in homogeneous light-driven systems, but also provides perspectives for the rational design of efficient but low-cost photosensitizers for solar fuel production.

Methods

Materials. All solvents and chemicals were commercially purchased and used as obtained without further purification, except for purpurin. Purpurin was recrystallized twice from absolute ethanol before usage.

Preparation of BIH. BIH was synthesized from a modified method based on the literature[64]. In total, 6.0 g of 2-phenylbenzimidazole was treated with 16 g of methyl iodide in 30 mL of methanol containing 1.28 g of NaOH. The reaction mixture was heated at 110 °C for 24 h to give a faint yellow solid (BIH^+I^-). The crude product was washed with H_2O to decolorize. The yield is over 80%. Then, a solution of BIH^+I^- in methanol was reduced by $NaBH_4$ (2 eq.) under N_2 to give a white solid (BIH). The white solid was purified by washing with $EtOH/H_2O$ (5:1, v/v). The yield is over 90%. The synthetic intermediates and target complexes were evidenced by ^1H NMR.

Preparation of chloro iron (III) 5,10,15,20-tetrakis (2′,6′-dihydroxyphenyl)-porphyrin. Chloro iron (III) 5,10,15,20-tetrakis (2′,6′-dihydroxyphenyl)-porphyrin was prepared following a reported procedure[62]. A solution of 2′–6′-dimethoxybenzaldehyde (1 g, 6.02 mmol) and pyrrole (0.419 mL, 602 mmol) in chloroform (600 mL) was degassed by argon for 20 min, then $BF_3·OEt_2$ (0.228 mL, 0.87 mmol) was added via a syringe. The solution was stirred under an inert atmosphere in the dark for 1.5 h, and 2,3-dichloro-5,6-dicyano-1,4-benzoquinone (DDQ) (1.02 g, 4.51 mmol) was added to the reaction. The mixture was stirred for an additional 1.5 h at reflux, cooled to room temperature, and 1 mL of triethylamine was added to neutralize the excessive acid. Then the solvent was removed, and the resulting black solid was purified by column chromatography (silica gel, dichloromethane) affording 5, 10, 15, 20-tetrakis(2′,6′-dimethoxyphenyl)-21H,23H-porphyrin as a purple powder (290 mg, 23%). To a solution of 5, 10, 15, 20-tetrakis(2′,6′-dimethoxyphenyl)-21H,23H-porphyrin (200 mg, 0.235 mmol) in dry dichloromethane (10 mL) at 0 °C was added BBr_3 (1000 μL, 10.38 mmol). The resulting green solution was stirred for 24 h at room temperature, then placed in ice water. Ethyl acetate was added to the suspension, and the mixture was washed with $NaHCO_3$. The organic layer was separated, washed twice with water, and then dried over anhydrous Na_2SO_4. The resulting solution was evaporated. The residue was purified by column chromatography (silica gel, 2:1 ethyl acetate/dichloromethane) to yield 5, 10, 15, 20-tetrakis(2′,6′-dihydroxyphenyl)-21H,23H-porphyrin as a purple powder (150 mg, 87%). Finally, a solution of 5, 10, 15, 20-tetrakis(2′,6′-dihydroxyphenyl)-21H,23H-porphyrin (100 mg, 0.135 mmol), $FeCl_2·4H_2O$ (270 mg, 1.35 mmol), and 2,6-lutidine (39 μL, 0.335 mmol) was heated at 50 °C and stirred for 3 h under an inert atmosphere in dry methanol. After methanol was removed, the resulting solid was dissolved in ethyl acetate, washed with 1.2 M HCl solution until pH was neutral. The crude product was purified by column chromatography (silica gel, ethyl acetate) to give chloro iron (III) 5,10,15,20-tetrakis (2′,6′-dihydroxyphenyl)-porphyrin as a brown solid (100 mg, 89%). The synthetic intermediates and target complexes were evidenced by ^1H NMR and HRMS spectroscopy.

Preparation of CuPP. A solution of $Cu(NO_3)_2·3H_2O$ (672 mg, 2.7 mmol) in DMF (5 mL) was added to a solution of purpurin (1380 mg, 5.4 mmol) in DMF (50 mL). The orange solution quickly turned into a brown suspension upon addition. Then a solution of $NaHCO_3$ (907 mg, 10.8 mmol) in H_2O (10 mL) was added to the reaction mixture with stirring for 24 h at 100 °C. After the mixture cooled down to room temperature, insoluble solids were removed by suction filtration. The filtrate was concentrated by rotary evaporation to ~10 mL, then excess diethyl ether was added, and the mixture was allowed to stir overnight at room temperature to precipitate out the product. A black precipitate ($Na_2Cu(PP)_2$) was collected under suction filtration, washed with diethyl ether (3 × 50 mL), and dried under vacuum (1.0 g, 60% yield). Anal. Calcd. for $C_{28}H_{12}CuO_{12}Na_2·2H_2O$: C, 51.43; H, 2.47; found: C, 51.26; H, 2.47. Cation exchange was carried out with the addition of tetrabutylammonium bromide (TBABr) (522 mg, 1.62 mmol, 2.0 equiv) to $Na_2Cu(PP)_2$ (500 mg, 0.81 mmol) in water at 60 °C for 6 h. The mixture was filtered and a brown solid was washed with water (3 × 10 mL) and then collected. Recrystallization of this compound from vapor diffusion of diethyl ether into an acetonitrile solution gave red crystals amenable to X-ray diffraction studies. The overall yield was 22%. ^1H MMR (400 MHz, d_6-DMSO, 25 °C): δ = 17.21, 8.18, 7.70, 7.54, 7.18, 6.64, 3.20–3.13, 1.57, 1.32–1.23, 0.93 ppm. All resonances are broad. Anal. Calcd. for $C_{60}H_{84}N_2O_{10}Cu$: C, 68.19; H, 8.01; N, 2.65; found: C, 67.94; H, 8.16; N, 2.60.

Characterization. ^1H and ^{13}C NMR spectra were recorded at a Bruker advance III 400-MHz NMR instrument. HRMS spectra were obtained on a Thermo Scientific Orbitrap Q Exactive ion trap mass spectrometer and QTOF-MS (Bruker Daltonics, times TOF). UV–vis spectra were determined on a Thermo Scientific GENESYS 50 UV–visible spectrophotometer. Elemental analyses were performed at an Elementar Vario EL analyzer. Dynamic light-scattering experiments were performed with a Brookhaven Elite Sizer zata-potential and a particle-size analyzer. Photoluminescence quantum yields were determined using a FLS 980 (Edinburgh instruments) absolute photoluminescence quantum yield measurement system and integrating sphere as a sample chamber. The steady-state fluorescence of solid samples was measured with FLS 920 fluorescence spectrometer (Edinburgh instruments).

X-ray crystallography. X-ray diffraction data were collected on SuperNova single-crystal diffractometer using the CuKα (1.54184 nm) radiation at 100 K. Absorption correction was carried out by a multiscan method. The crystal structure was solved by direct methods with SHELXT[65] program, and was refined by full-matrix least-square methods with SHELXL[65] program contained in the Olex2 suite[66]. Weighted R factor (Rw) and the goodness of fit S were based on F_2, conventional R factor(R) was based on F (Supplementary Table 9). Hydrogen atoms were placed with the AFIX instructions and were refined using a riding mode. Figures were drawn with Diamond software. Details can be obtained from the Cambridge Crystallographic Data Centre at www.ccdc.cam.ac.uk for CCDC accession number 2017326.

Cyclic voltammetry. Cyclic voltammetry (CV) measurements were performed with a CHI-760E electrochemical analyzer using a one-compartment cell with a glassy carbon disk working electrode (diameter 3 mm), Pt auxiliary electrode, and a SCE reference electrode. The electrolyte solutions were 0.1 M tetrabutylammonium hexafluorophosphate in DMF. Solutions were purged with N_2 or CO_2 over 30 min before measurements. All reported potentials in this work are versus SCE.

Fluorescence quenching. A solution of photosensitizer was degassed by N_2 for 15 min in a sealed quartz cuvette with a septum cap. Different concentrations of BIH or catalyst were added to the solution of photosensitizer under N_2. The steady-state fluorescence for solution samples was measured by Duetta fluorescence and absorbance spectrometer. The excited-state lifetime (τ_0) of CuPP and PP was measured with an FLS 920 fluorescence spectrometer (Edinburgh instruments), in which a picosecond pulsed diode laser (λ = 472 nm) (Edinburgh instruments EPL-470) was used as the excitation source. The quenching rate constant (k_q) was calculated by Stern–Volmer equation:

$$I_0/I \text{ or } \tau_0/\tau = 1 + k_q \times \tau_0 \times [Q] \tag{1}$$

where I_0 and I represent the fluorescence intensity of photosensitizer in the absence and presence of quencher, k_q is the quenching rate constant, τ_0 is the lifetime of the photosensitizer, and [Q] is the concentration of quencher.

Photocatalytic CO_2 reduction. Photocatalytic experiments were conducted in a closed scintillation vial with rubber plug and magnetic stirring. The headspace of the vial was 53.4 mL. A reaction mixture (5.0 mL) was bubbled with CO_2 for 25 min and then irradiated with a white LED light setup (λ > 400 nm, PCX-50B/50 C, Beijing Perfectlight Technology Co., Ltd.). The gaseous products were analyzed by Shimadzu GC-2014 gas chromatography equipped with Shimadzu Molecular Sieve 13 × 80/100 3.2 × 2.1 mm × 3.0 m and Porapak N 3.2 × 2.1 mm × 2.0-m columns. A thermal conductivity detector (TCD) was used to detect H_2 and a flame ionization detector (FID) with a methanizer was used to detect CO and other hydrocarbons. Nitrogen was used as the carrier gas. The oven temperature was kept at 60 °C. The TCD detector and injection port were kept at 100 and 200 °C, respectively. ^{13}C isotopic labeling experiments were carried out in a $^{13}CO_2$ atmosphere and gas products were detected by GC–MS (Agilent 7890A-5975C). HPLC (HP1100, Hewlett Packard) was used to analyze the photolysis products in the solution.

Quantum yield measurement. The difference between the power of light passing through the blank (containing FeTDHPP and BIH) and through the sample (containing CuPP, FeTDHPP, and BIH) was used to calculate the light absorbed by the CuPP. The average intensity of the irradiation P (W/cm^2) was measured with a FZ-A Power meter (Beijing Normal University Optical Instrument company). The monochromic light of 450 nm obtained using blue LED light setup (λ = 450 nm, PCX-50B/50C, Beijing Perfectlight Technology Co., Ltd.). Generally, the quantum yield for CO_2 reduction to CO was calculated after irradiation for 1 h at 450 nm using the following equation:

$$\Phi_{CO} = \frac{2 \times \text{number of the CO molecules}}{\text{number of incident photons}} \times 100\% \tag{2}$$

that is,

$$\Phi_{CO} = \frac{2 \times n(CO)}{I} \times 100\% \tag{3}$$

where $n(CO)$ is the number of molecules of CO produced, I is the number of incident photons; the calculation formula of the incident photon number I is as follows:

$$I = PSt\frac{\lambda}{hc} \tag{4}$$

where S is the incident irradiation area ($S = 0.785$ cm^2), t is the irradiation time, λ is the incident wavelength, h is the Plank constant (6.626×10^{-34} J·s), and c is the speed of light (3×10^8 m s^{-1})

$$\Phi = \frac{2 \times n \times N_A}{PSt \times \frac{\lambda}{hc}} \times 100\% \qquad (5)$$

where N_A is the Avogadro constant (6.02×10^{23} mol^{-1}).

Data availability

The data that support the findings of this study are available from the corresponding author on reasonable request. The X-ray crystallographic coordinates for structures reported in this study have been deposited at the Cambridge Crystallographic Data Centre (CCDC), under deposition numbers 2017326. These data can be obtained free of charge from The Cambridge Crystallographic Data Centre via www.ccdc.cam.ac.uk/data_request/cif. Source data are provided with this paper.

References

1. Nocera, D. G. Chemistry of personalized solar energy. *Inorg. Chem.* **48**, 10001–10017 (2009).
2. Gray, H. B. Powering the planet with solar fuel. *Nat. Chem.* **1**, 7–7 (2009).
3. Lewis, N. S. & Nocera, D. G. Powering the planet: chemical challenges in solar energy utilization. *Proc. Natl Acad. Sci. USA* **103**, 15729–15735 (2006).
4. Appel, A. M. et al. Frontiers, opportunities, and challenges in biochemical and chemical catalysis of CO_2 fixation. *Chem. Rev.* **113**, 6621–6658 (2013).
5. Hepburn, C. et al. The technological and economic prospects for CO_2 utilization and removal. *Nature* **575**, 87–97 (2019).
6. Wang, Z.-j, Song, H., Liu, H. & Ye, J. Coupling of solar energy and thermal energy for carbon dioxide reduction: status and prospects. *Angew. Chem. Int. Ed.* **59**, 8016–8035 (2020).
7. Bushuyev, O. S. et al. What should we make with CO_2 and how can we make it? *Joule* **2**, 825–832 (2018).
8. Morris, A. J., Meyer, G. J. & Fujita, E. Molecular approaches to the photocatalytic reduction of carbon dioxide for solar fuels. *Acc. Chem. Res.* **42**, 1983–1994 (2009).
9. Gao, C., Wang, J., Xu, H. & Xiong, Y. Coordination chemistry in the design of heterogeneous photocatalysts. *Chem. Soc. Rev.* **46**, 2799–2823 (2017).
10. Luo, Y.-H., Dong, L.-Z., Liu, J., Li, S.-L. & Lan, Y.-Q. From molecular metal complex to metal-organic framework: the CO_2 reduction photocatalysts with clear and tunable structure. *Coord. Chem. Rev.* **390**, 86–126 (2019).
11. Yamazaki, Y., Takeda, H. & Ishitani, O. Photocatalytic reduction of CO_2 using metal complexes. *J. Photochem. Photobiol. C.* **106–137** (2015).
12. Dalle, K. E. et al. Electro- and solar-driven fuel synthesis with first row transition metal complexes. *Chem. Rev.* **119**, 2752–2875 (2019).
13. Sampaio, R. N., Grills, D. C., Polyansky, D. E., Szalda, D. J. & Fujita, E. Unexpected roles of triethanolamine in the photochemical reduction of CO_2 to formate by rutheniumcomplexes. *J. Am. Chem. Soc.* **142**, 2413–2428 (2020).
14. Shirley, H. et al. Durable solar-powered systems with Ni-catalysts for conversion of CO_2 or CO to CH_4. *J. Am. Chem. Soc.* **141**, 6617–6622 (2019).
15. Hong, D. et al. Efficient photocatalytic CO_2 reduction by a Ni(II) complex having pyridine pendants through capturing a Mg^{2+} ion as a Lewis-acid cocatalyst. *J. Am. Chem. Soc.* **141**, 20309–20317 (2019).
16. Cheung, P. L., Kapper, S. C., Zeng, T., Thompson, M. E. & Kubiak, C. P. Improving photocatalysis for the reduction of CO_2 through non-covalent supramolecular assembly. *J. Am. Chem. Soc.* **141**, 14961–14965 (2019).
17. Ouyang, T. et al. Dinuclear metal synergistic catalysis boosts photochemical CO_2-to-CO conversion. *Angew. Chem. Int. Ed.* **57**, 16480–16485 (2018).
18. Kamada, K. et al. Photocatalytic CO_2 reduction using a robust multifunctional iridium complex toward the selective formation of formic acid. *J. Am. Chem. Soc.* **142**, 10261–10266 (2020).
19. Lee, S. K. et al. Function-integrated Ru catalyst for photochemical CO_2 reduction. *J. Am. Chem. Soc.* **140**, 16899–16903 (2018).
20. Rao, H., Schmidt, L. C., Bonin, J. & Robert, M. Visible-light-driven methane formation from CO_2 with a molecular iron catalyst. *Nature* **548**, 74–77 (2017).
21. Hameed, Y., Berro, P., Gabidullin, B. & Richeson, D. An integrated Re(II) photocatalyst/sensitizer that activates the formation of formic acid from reduction of CO_2. *Chem. Commun.* **55**, 11041–11044 (2019).
22. Liyanage, N. P. et al. Photochemical CO_2 reduction with mononuclear and dinuclear rhenium catalysts bearing a pendant anthracene chromophore. *Chem. Commun.* **55**, 993–996 (2019).
23. Genoni, A. et al. Tuning iridium photocatalysts and light irradiation for enhanced CO_2 reduction. *ACS Catal.* **7**, 154–160 (2017).
24. Thoi, V. S., Kornienko, N., Margarit, C. G., Yang, P. & Chang, C. J. Visible-light photoredox catalysis: selective reduction of carbon dioxide to carbon monoxide by a nickel N-heterocyclic carbene–isoquinoline complex. *J. Am. Chem. Soc.* **135**, 14413–14424 (2013).
25. Fogeron, T., Retailleau, P., Chamoreau, L.-M., Li, Y. & Fontecave, M. Pyranopterin related dithiolene molybdenum complexes as homogeneous catalysts for CO_2 photoreduction. *Angew. Chem. Int. Ed.* **57**, 17033–17037 (2018).
26. Liu, D.-C., Zhong, D.-C. & Lu, T.-B. Non-noble metal-based molecular complexes for CO_2 reduction: From the ligand design perspective. *EnergyChem* **2**, 100034 (2020).
27. Matsuoka, S. et al. Efficient and selective electron mediation of cobalt complexes with cyclam and related macrocycles in the p-terphenyl-catalyzed photoreduction of carbon dioxide. *J. Am. Chem. Soc.* **115**, 601–609 (1993).
28. Grodkowski, J. et al. Reduction of cobalt and iron corroles and catalyzed reduction of CO_2. *J. Phys. Chem. A* **106**, 4772–4778 (2002).
29. Shipp, J. D. et al. Sterically hindered Re- and Mn-CO_2 reduction catalysts for solar energy conversion. *Dalton Trans.* **49**, 4230–4243 (2020).
30. Gollnick, K. & Held, S. Hydroxyanthraquinones as sensitizers of electron-transfer-induced photo-oxygenation reactions. *J. Photochem. Photobiol. A: Chem.* **70**, 135–145 (1993).
31. Han, Z. & Eisenberg, R. Fuel from water: the photochemical generation of hydrogen from water. *Acc. Chem. Res.* **47**, 2537–2544 (2014).
32. Bonin, J., Robert, M. & Routier, M. Selective and efficient photocatalytic CO_2 reduction to CO using visible light and an iron-based homogeneous catalyst. *J. Am. Chem. Soc.* **136**, 16768–16771 (2014).
33. Guo, Z. et al. Highly efficient and selective photocatalytic CO_2 reduction by iron and cobalt quaterpyridine complexes. *J. Am. Chem. Soc.* **138**, 9413–9416 (2016).
34. Rao, H., Bonin, J. & Robert, M. Visible-light homogeneous photocatalytic conversion of CO_2 into CO in aqueous solutions with an iron catalyst. *ChemSusChem* **10**, 4447–4450 (2017).
35. Chen, L. et al. A molecular noble metal-free system for efficient visible light-driven reduction of CO_2 to CO. *Dalton Trans.* **48**, 9596–9602 (2019).
36. Zhang, Y., Schulz, M., Wächtler, M., Karnahl, M. & Dietzek, B. Heteroleptic diimine–diphosphine Cu(I) complexes as an alternative towards noble-metal based photosensitizers: design strategies, photophysical properties and perspective applications. *Coord. Chem. Rev.* **356**, 127–146 (2018).
37. Takeda, H., Ohashi, K., Sekine, A. & Ishitani, O. Photocatalytic CO_2 reduction using Cu(I) photosensitizers with a Fe(II) catalyst. *J. Am. Chem. Soc.* **138**, 4354–4357 (2016).
38. Rosas-Hernández, A., Steinlechner, C., Junge, H. & Beller, M. Earth-abundant photocatalytic systems for the visible-light-driven reduction of CO_2 to CO. *Green. Chem.* **19**, 2356–2360 (2017).
39. Sakaguchi, Y., Call, A., Cibian, M., Yamauchi, K. & Sakai, K. An earth-abundant system for light-driven CO_2 reduction to CO using a pyridinophane iron catalyst. *Chem. Commun.* **55**, 8552–8555 (2019).
40. Zhang, X., Cibian, M., Call, A., Yamauchi, K. & Sakai, K. Photochemical CO_2 reduction driven by water-soluble copper(I) photosensitizer with the catalysis accelerated by multi-electron chargeable cobalt porphyrin. *ACS Catal.* **9**, 11263–11273 (2019).
41. Gracia, L.-L. et al. New photosensitizers based on heteroleptic Cu^I complexes and CO_2 photocatalytic reduction with [Ni^{II}(cyclam)]Cl2. *Chem. Eur. J.* **26**, 9929–9937 (2020).
42. Takeda, H. et al. Highly efficient and robust photocatalytic systems for CO_2 reduction consisting of a Cu(I) photosensitizer and Mn(I) catalysts. *J. Am. Chem. Soc.* **140**, 17241–17254 (2018).
43. Steinlechner, C. et al. Selective earth-abundant system for CO_2 reduction: comparing photo- and electrocatalytic processes. *ACS Catal.* **9**, 2091–2100 (2019).
44. Kuramochi, Y., Fujisawa, Y. & Satake, A. Photocatalytic CO_2 reduction mediated by electron transfer via the excited triplet state of Zn(II) porphyrin. *J. Am. Chem. Soc.* **142**, 705–709 (2020).
45. Kuramochi, Y. & Satake, A. Photocatalytic CO_2 reductions catalyzed by meso-(1,10-phenanthrolin-2-yl)-porphyrins having a rhenium(I) tricarbonyl complex. *Chem. Eur. J.* **26**, 16365–16373 (2020).
46. Yamazaki, Y. & Ishitani, O. Synthesis of Os(II)–Re(I)–Ru(II) hetero-trinuclear complexes and their photophysical properties and photocatalytic abilities. *Chem. Sci.* **9**, 1031–1041 (2018).
47. Pierpont, C. G. Studies on charge distribution and valence tautomerism in transition metal complexes of catecholate and semiquinonate ligands. *Coord. Chem. Rev.* **216-217**, 99–125 (2001).
48. Call, A. et al. Highly efficient and selective photocatalytic CO_2 reduction to CO in water by a cobalt porphyrin molecular catalyst. *ACS Catal.* **9**, 4867–4874 (2019).

49. Matíes, R., Jiménez, F., Arias, J. J. & Román, M. Spectrofluorimetric determination of zinc with 1,2,4-trihydroxyanthraquinone in pharmaceutical preparations. *Anal. Let.* **30**, 2059–2070 (1997).

50. Capitán, F., Ramirez, A. A. & Linares, C. J. Spectrophotometric determination of trace amounts of iron(III) in salicylates by extraction of the mixed-ligand iron-salicylate-purpurin complex. *Analyst* **111**, 739–741 (1986).

51. Churchill, M. R. et al. Linkage and redox isomerism in ruthenium complexes of catecholate, semi-quinone, and o-acylphenolate ligands derived from tri- and tetrahydroxy-9,10-anthracenediones. *Inorg. Chem.* **40**, 4361–4367 (2001).

52. Di Vaira, M., Orioli, P., Piccioli, F., Bruni, B. & Messori, L. Structure of a terbium(III)−quinizarine complex: the first crystallographic model for metalloanthracyclines. *Inorg. Chem.* **42**, 3157–3159 (2003).

53. Das, P. et al. Synthesis, crystal structure, DNA interaction and in vitro anticancer activity of a Cu(II) complex of purpurin: dual poison for human DNA topoisomerase I and II. *RSC Adv.* **4**, 59344–59357 (2014).

54. Miliani, C., Romani, A. & Favaro, G. Acidichromic effects in 1,2-di- and 1,2,4-tri- hydroxyanthraquinones. A spectrophotometric and fluorimetric study. *J. Phys. Org. Chem.* **13**, 141–150 (2000).

55. Grazia, C., Clementi, C., Miliani, C. & Romani, A. Photophysical properties of alizarin and purpurin Al(III) complexes in solution and in solid state. *Photochem. Photobiol. Sci.* **10**, 1249–1254 (2011).

56. Miliani, C., Romani, A. & Favaro, G. A spectrophotometric and fluorimetric study of some anthraquinoid and indigoid colorants used in artistic paintings. *Spectrochim. Acta A* **54**, 581–588 (1998).

57. McMillin, D. R. & McNett, K. M. Photoprocesses of copper complexes that bind to DNA. *Chem. Rev.* **98**, 1201–1220 (1998).

58. Hossain, A. et al. Visible-light-accelerated copper(II)-catalyzed regio- and chemoselective oxo-azidation of vinyl arenes. *Angew. Chem. Int. Ed.* **57**, 8288–8292 (2018).

59. Li, Y. et al. Copper(II)-catalyzed asymmetric photoredox reactions: enantioselective alkylation of imines driven by visible light. *J. Am. Chem. Soc.* **140**, 15850–15858 (2018).

60. Luo, S. P. et al. Photocatalytic water reduction with copper-based photosensitizers: a noble-metal-free system. *Angew. Chem. Int. Ed.* **125**, 437–441 (2013).

61. Nagaoka, T., Nishii, N., Fujii, K. & Ogura, K. Mechanisms of reductive addition of CO_2 to quinones in acetonitrile. *J. Electroanal. Chem.* **322**, 383–389 (1992).

62. Costentin, C., Drouet, S., Robert, M. & Savéant, J.-M. A local proton source enhances CO_2 electroreduction to CO by a molecular Fe catalyst. *Science* **338**, 90–94 (2012).

63. Kuramochi, Y., Kamiya, M. & Ishida, H. Photocatalytic CO_2 reduction in n,n-dimethylacetamide/water as an alternative solvent system. *Inorg. Chem.* **53**, 3326–3332 (2014).

64. Zhu, X.-Q., Zhang, M.-T., Yu, A., Wang, C.-H. & Cheng, J.-P. Hydride, hydrogen atom, proton, and electron transfer driving forces of various five-membered heterocyclic organic hydrides and their reaction intermediates in acetonitrile. *J. Am. Chem. Soc.* **130**, 2501–2516 (2008).

65. Sheldrick, G. A short history of SHELX. *Acta Cryst.* **A64**, 112–122 (2008).

66. Dolomanov, O. V., Bourhis, L. J., Gildea, R. J., Howard, J. A. K. & Puschmann, H. OLEX2: a complete structure solution, refinement and analysis program. *J. Appl. Cryst.* **42**, 339–341 (2009).

Competing interests
The authors declare no competing interests.

Additional information
Supplementary information The online version contains supplementary material available at https://doi.org/10.1038/s41467-021-21923-9.

Correspondence and requests for materials should be addressed to Z.H.

Peer review information *Nature Communications* thanks Claudia Bizzarri, Tai-Chu Lau, and other, anonymous, reviewers for their contributions to the peer review of this work. Peer review reports are available.

Reprints and permission information is available at http://www.nature.com/reprints

Publisher's note Springer Nature remains neutral with regard to jurisdictional claims in published maps and institutional affiliations.